Bulletin of the Seismological Society of America, Vol. 104, No. 3, pp. 1276–1288, June 2014, doi: 10.1785/0120130157

Correction of Ocean-Bottom Seismometer Instrumental Clock Errors Using Ambient Seismic Noise

by Pierre Gouédard,* Tim Seher, Jeffrey J. McGuire, John A. Collins, and Robert D. van der Hilst

Abstract Very accurate timing of seismic recordings is critical for modern processing techniques. Clock synchronization among the instruments constituting an array is, however, difficult without direct communication between them. Synchronization to Global Positioning System (GPS) time is one option for on-land deployments, but not for underwater surveys as electromagnetic signals do not propagate efficiently in water. If clock drift is linear, time corrections for ocean-bottom seismometer (OBS) deployments can be estimated through GPS synchronization before and after the deployment, but this is not sufficient for many applications as the nonlinear component of the drift can reach tens to hundreds of milliseconds for long-duration experiments. We present two techniques to retrieve timing differences between simultaneous recordings at ocean-bottom instruments after deployment has ended. Both techniques are based on the analysis of the cross correlation of ambient seismic noise and are effective even if clock drift is nonlinear. The first, called time symmetry analysis, is easy to apply but requires a proper illumination so that the noise cross-correlation functions are symmetric in time. The second is based on the doublet analysis method and does not have this restriction. Advantages and drawbacks of both approaches are discussed. Application to two OBS data sets shows that both can achieve synchronization of recordings down to about five milliseconds (a few percent of the main period used).

Introduction

As a result of better instruments, larger and denser receiver arrays, and increasing computational power, geophysical images of the ground are becoming more and more detailed. In earthquake studies, for instance, it is now common to determine the differential arrival time between two earthquakes with waveform cross correlation (the so-called double-difference techniques) to a precision approaching one tenth of a sample (Rubin *et al.*, 1999). The combination of these measurement techniques with relative location algorithms has produced a 1–2 order of magnitude increase in location precision compared with standard seismic catalogs and allows high-resolution studies of fault zones (Rubin and Gillard, 2000; Schaff *et al.*, 2002, 2004; Lin *et al.*, 2008). This type of analysis routinely detects timing errors on the order of 10–50 ms in standard monitoring networks (Rubin, 2002; Lin *et al.*, 2008). On land, datalogger clocks can be synchronized to Global Positioning System (GPS) time and time errors that do occur result mainly from changes to the electronic equipment at particular stations.

For typical ocean-bottom seismometer (OBS) deployments, the problem is much worse because the clocks are only synchronized to GPS time before and after deployments, which can last up to several years. Clocks in modern OBSs typically have drift rates of half a second per year, but these can be up to several seconds per year (Fig. 1; Gardner and Collins, 2012). The instrument clock can be synchronized to GPS time prior to deployment, and the offset from GPS time is measured immediately after recovery, which allows a linear drift to be removed from the data set. Figure 1 shows the estimates of this linear drift rate from pre/post deployment GPS fixes for Woods Hole Oceanographic Institution instruments covering a total of more than 150 on-bottom years. The drift rates routinely have values larger than 1 s per year. Although the linear part of the drift can be straightforwardly removed, there is a substantial nonlinear component to the clock drift that remains in the data (Gardner and Collins, 2012). OBS studies of microearthquakes on both the Mid-Atlantic Ridge (deMartin *et al.*, 2007; Düsünür *et al.*, 2009) and the East Pacific Rise (EPR) (Tolstoy *et al.*, 2008) have recorded exceedingly abundant microseismicity. These data sets are recorded at frequencies of up to a few hundred Hz and require location accuracy on the order of tens of

*Now at Magnitude LLC, a Baker Hughes and CGG joint venture, Centre Regain, 04220 Sainte Tulle, France.

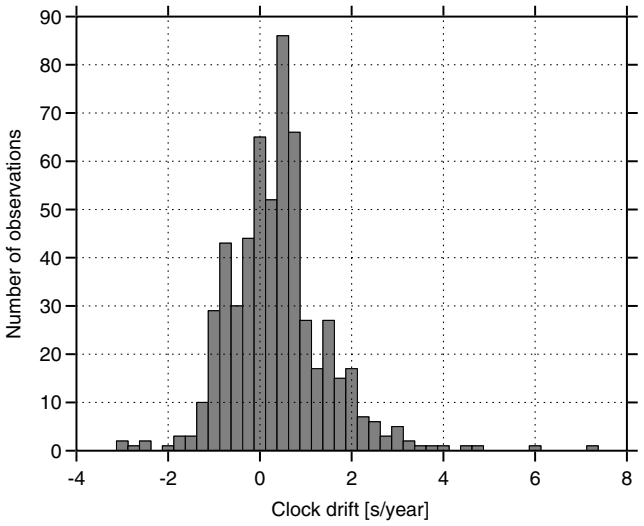

Figure 1. Clock performance of the Woods Hole Oceanographic Institution Ocean-Bottom Seismometers (OBSs) Instrument Pool, measured over ~700 deployments (~100 are year-long passive deployments and others are $\lesssim$ one-month active-source deployments) for a total of more than 150 on-bottom years. The drift rates are routinely above 1 s per year (see also Gardner and Collins, 2012).

meters to study processes such as the time dependence of hydrothermal fluid flow (Tolstoy *et al.*, 2008; Stroup *et al.*, 2009). Moreover, the magnitude of residuals found in waveform-based earthquake location studies using OBS data, ~50 ms (McGuire *et al.*, 2012), is significantly less than the total clock drift over year long experiments. Thus, any clock drift that is not properly corrected in OBS data will be a limiting factor in high-precision earthquake locations and associated tomographic inversions for velocity structure. Many data sets that include these types of errors are already archived at the Incorporated Research Institution for Seismology (IRIS) data management center and more are routinely being collected by the National Science Foundation's OBS Instrument Pool.

We investigate two methods for synchronizing clocks between instruments among an array, based on the continuous recording of seismic ambient noise: time symmetry analysis (TSA) (Stehly *et al.*, 2007; Sens-Schönfelder, 2008) and a virtual doublet method, adapted to ambient noise processing from the seismic doublet technique (Poupinet *et al.*, 1984, 2008). This latter technique was not initially developed to infer clock differences, but we found it is efficient at doing so. We use two data sets to illustrate the application of these techniques in real case scenarios. The first one, the Sismomar experiment (Singh *et al.*, 2006; Crawford *et al.*, 2010), is a short-term (20 days) active-source survey. The second data set is a passive one-year-long deployment aimed at studying earthquake sources at the Quebrada–Discovery–Gofar (QDG) transform fault system on the EPR (McGuire *et al.*, 2012).

Two time scales will be used in this paper: the short one corresponds to the time in the records, whereas the long one corresponds to calendar date. The goal of this work is to characterize instrument time errors (clock errors), that is, fluctuations on the short time scale as a function of the long one. The total clock errors are considered to be composed of a dynamic and a static time shift. The dynamic time shift is the part that fluctuates over dates (the drift) and is defined within a constant. It can be viewed as the timing error with respect to an arbitrary date. The static time shift is constant over dates, and adding it to the dynamic shift yields an absolute error.

Although the analysis presented here focuses on the correction of OBS instrumental errors, the methods described in the following are fully applicable (and have to some extent already been successfully applied) to land seismic experiments (see for instance Stehly *et al.*, 2007, and Sens-Schönfelder, 2008, for applications of TSA).

Methods

Timing Errors from Time Symmetry Analysis

The cross correlation of a diffuse field, recorded at two receivers, yields the Green's function of the medium between these receivers (e.g., Weaver and Lobkis, 2001; Campillo and Paul, 2003; Shapiro and Campillo, 2004; Wapenaar, 2004; Weaver, 2005; Campillo, 2006; Larose *et al.*, 2006). For a fully isotropic, equipartitioned field, this recovery is perfect (Sánchez-Sesma and Campillo, 2006; Sánchez-Sesma *et al.*, 2006; Gouédard, Stehly, *et al.*, 2008). In practice, the cross correlation only allows a partial recovery of the Green's function (Gouédard, Roux, *et al.*, 2008; Weaver *et al.*, 2009; Yao *et al.*, 2009; Froment *et al.*, 2010), which we will refer to as noise cross-correlation function (NCCF). In the best-case scenario, the NCCF is a band-limited, surface-wave-enhanced version of the Green's function. Such an NCCF is antisymmetric in time, with positive and negative times corresponding to causal and acausal waveforms, respectively, which are identical in a reciprocal medium. If the recorded wavefield is not isotropic but has a smooth azimuthal energy density function, the amplitudes in the causal and acausal parts may differ, but the positive and negative travel times stay (almost) equal (Tsai, 2009; Weaver *et al.*, 2009; Yao and van der Hilst, 2009; Froment *et al.*, 2010). In the worst-case scenario, this phase symmetry is broken and the causal and acausal travel times are different. This can either be due to different properties of the incident wavefields in the two opposite directions defined by the pair of receivers, or from timing errors at at least one of the receivers. Stehly *et al.* (2007) suggested that one can discriminate between these two effects by looking at the evolution of the asymmetry with the date: the noise coming from opposite directions is unlikely to evolve exactly the same way, and the difference between the positive and the negative travel times will not stay constant over the long time scale (see also Sens-Schönfelder, 2008). On the other hand, clock errors will affect positive and negative travel times in an opposite manner, and their differences will remain the

same. We will use this first method, referred to as TSA of the NCCFs, in this part of the paper to infer instrumental time shifts in the data from continuous recordings after ensuring all variations of arrival times in NCCFs are related to instrumental errors and not to a variation of the illumination. Note the data sets used here have two main differences compared with previous work by Stehly *et al.* (2007) and Sens-Schönfelder (2008). First, TSA will be applied to experiments at sea using OBSs. Second, one of the two surveys was an active source experiment (but with continuous recording) and air-gun signals are present in the data (which we will show do not affect our measurements).

The positive-time and negative-time waveforms for a daily NCCF, windowed around the direct surface-wave arrival, are denoted as $s^+(t)$ and $s^-(t)$, respectively (which means the complete windowed waveform can be written as $s(t) = s^+(t) + s^-(-t)$ with $s^+(-t) = 0$ and $s^-(+t) = 0$ for $t > 0$). An easy procedure to measure the absolute clock difference $\delta t_{ss}^{\text{abs}}$ between two stations would be to locate the center of the positive- and negative-side peaks in $s(t)$. $\delta t_{ss}^{\text{abs}}$ would then be measured by picking the maximum of the cross-correlations $s^+ \otimes s^-$. This would in practice not be very effective, however, because this would require $s^+(t)$ and $s^-(t)$ to have similar waveforms, which in turn usually requires the use of longer recording times in the cross-correlation process. A better procedure is to first infer a timing error relative to an arbitrary reference (the aforementioned dynamic time shift) and convert this to an absolute error afterward:

1. For each pair of stations, the daily NCCFs are averaged to form a reference trace $r(t)$, which is decomposed into $r^+(t)$ and $r^-(t)$ similarly to what was described for $s(t)$. The time shifts dt^+ and dt^- (both positive numbers) for the positive and negative sides are inferred from the cross-correlations $r^+ \otimes s^+$ and $r^- \otimes s^-$, respectively. A confidence interval is defined as the lag time range for which the correlation coefficient is above 90% of its maximum value, and the width of this interval is used as an estimate of the measurement error. The dynamic timing error is obtained following $\delta t^{\text{dyn}} = (dt^+ - dt^-)/2$. As detailed in Stehly *et al.* (2007), the difference $dt^+ - dt^-$ is not affected by variations of the medium wavespeed, if any, because these affect dt^+ and dt^- in a symmetric way.
2. Because the reference $r(t)$ was built from a stack of potentially misaligned NCCFs it must itself contain errors. Therefore, measured time shifts δt^{dyn} from the first step are corrected for, and a new reference is computed and used in a second iteration of step 1 above. The number of iterations needed to reach a targeted level of accuracy in δt^{dyn} depends on the amplitude of the timing errors and the signal-to-noise ratio of the NCCFs, but measurements usually converge after a few iterations.
3. The procedure described above gives a measurement of clock differences between pairs of stations, for each day, relative to the arbitrary reference. This relative measurement δt^{dyn} can be made absolute by evaluating the timing error in the reference. This static error δt^{stat} is obtained from the cross-correlation $r^+ \otimes r^-$ (which maximum should be at zero lag time in an ideal situation with no timing errors and perfectly symmetric NCCFs), and the absolute timing error is obtained as $\delta t^{\text{abs}} = \delta t^{\text{dyn}} + \delta t^{\text{stat}}$.
4. The last step consists of deriving the timing error at each station of the array, relative to a master station, from the clock differences between each pair of stations. This is done using a least-squares inversion (e.g., Tarantola, 2005), which allows the regularization of the results and takes into account the aforementioned measurement errors on the time shifts through a data covariance matrix. The regularization we used here forces the second-order derivative of the time error with respect to the date to be small using an appropriate model covariance matrix (e.g., Constable *et al.*, 1987), thus providing smooth error versus date curves.

δt^{stat}, measured on the reference during step 3, is more accurate than $\delta t_{ss}^{\text{abs}}$ described previously, even if obtained using the exact same procedure, because $r^+(t)$ and $r^-(t)$ are more likely to have similar waveforms than $s^+(t)$ and $s^-(t)$ because of the long term averaging.

Precision on the static error δt^{stat} is not as good as on the relative error δt^{dyn}, because even the stacked NCCF might not have converged toward a symmetric waveform. This precision can be assessed using the closure relations between triplets of stations (Stehly *et al.*, 2007). For any three stations A, B, and C, the clock differences $\delta t_{AB}^{\text{abs}}$, $\delta t_{BC}^{\text{abs}}$, and $\delta t_{AC}^{\text{abs}}$ between each pair must satisfy the closure relation $\delta t_{AB}^{\text{abs}} + \delta t_{BC}^{\text{abs}} - \delta t_{AC}^{\text{abs}} = 0$ at all dates. This relation is not satisfied in practice, and the amplitude of the residuals can be used as an error estimate for the static error. When considering a large number of stations, using the closure relations between all combinations of three stations as an additional constraint during the inversion (step 4 above) can help reduce the error on the static time shift for each pair, assuming the error on the dynamic shifts is small compared with the one on the static shifts.

Having a clock reference at one moment for one station (e.g., from a GPS for land seismic or assuming no error at deployment time for OBS setup) provides a ground truth reference, which suppresses both the need of static time-shift estimates from the reference and the need to define timing errors at all stations with respect to one. One then recovers the absolute timing errors at each station at the accuracy of the dynamic time shift.

We note that dt^+ and dt^-, defined above as the picked arrival times of the direct waves, form the positive and the negative time of the NCCF, respectively, could be defined as the arrival time of any wave (direct, reflected, or refracted *P* or *S* body wave, surface wave, etc.), as long as one can ensure it is the same wave that is picked on both sides of the NCCF. This allows for selecting the more convenient wave packet (usually the more energetic), depending on the considered deployment.

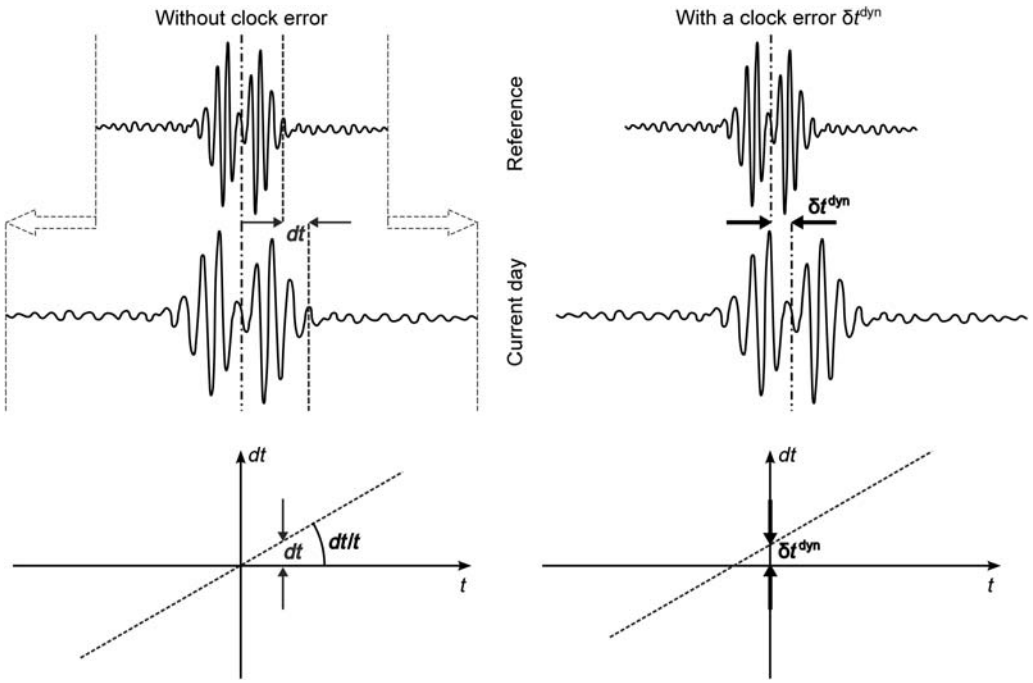

Figure 2. Illustration of the virtual doublet method. A current day NCCF is compared with a reference by measuring shifts dt between the waveforms in a moving window centered on t (top left). The dt/t stretching coefficient is inferred from the dt versus t plot (bottom left). If there is a timing difference δt^{dyn} (right column), the current day NCCF is shifted by this amount. The slope dt/t is not affected in the dt versus t plot (bottom right), and δt^{dyn} can be inferred. δt^{dyn} can be measured even if $dt/t = 0$.

Timing Errors Using Virtual Doublet Analysis

A limitation of the TSA method is the requirement that the NCCF converges toward something sufficiently similar to the true Green's function so that both $s^+(t)$ and $s^-(t)$ have a stable peak and these peaks have similar waveforms (at least in the long-term averaged NCCF $r(t)$). If these peaks have different waveforms, but are still above the noise level in the NCCF, the relative timing error δt^{dyn} can be evaluated; however, the static δt^{stat} cannot be evaluated because the correlation $r^+ \otimes r^-$ will not have a well-defined peak. If the NCCFs are one sided, much stronger assumptions have to be made to retrieve timing errors from only one of dt^+ or dt^-. These error estimates cannot be distinguished from temporal changes in the medium properties or from variations in the noise wavefield, because the symmetry of the variations of dt^+ versus dt^- over the long time scale cannot be assessed (Stehly *et al.*, 2007). In particular, any fluctuation of the travel time due to a change in the medium can be misinterpreted as a drift of the clock. In the next paragraph, we introduce an alternative method that overcomes these limitations.

Our proposed procedure is based on the doublet technique developed by Poupinet *et al.* (1984) and recently adapted to ambient noise processing (Sens-Schönfelder and Wegler, 2006; Wegler and Sens-Schönfelder, 2007; Brenguier, Campillo, *et al.*, 2008; Brenguier, Shapiro, *et al.*, 2008; Poupinet *et al.*, 2008), hence the virtual doublet name. The primary goal of this method is to monitor temporal velocity variations in the medium by looking for stretching of the NCCF waveforms computed at different dates. The virtual doublet method is well established, so we only illustrate that the accuracy of this method for determining velocity changes is not affected by timing errors in the data and that the method can be used to measure those timing errors.

The virtual doublet method, applied to noise recordings, compares a current day NCCF (obtained from short duration noise records—usually on the order of one month for regional studies—centered on the current date) to a reference (usually an averaged NCCF over a longer time period, typically on the order of one year or more). The objective is to measure any stretching between the waveforms, which would correspond to a homogeneous change in the velocity. This is done by measuring time shifts dt between the two waveforms in a moving time window centered on t (Fig. 2, left). A homogeneous relative variation dv/v of the medium's wavespeed results in one waveform being a stretched version of the other such that dt is a linear function of t. dt/t is then estimated by linear regression and is interpreted as being equal to the opposite of a spatially homogeneous dv/v. The stretching coefficient dt/t can be measured with a resolution on the order of 10^{-4}, especially if the measurement error of each dt is used to weigh each point in the regression (e.g., Clarke *et al.*, 2011). If there is a timing difference δt^{dyn} between the two stations, each current day NCCF is shifted by this amount, and each of the dt are increased by δt^{dyn} (Fig. 2, top right). The slope dt/t is not affected by such a change, hence measurements of velocity variations made with the virtual doublet method are

insensitive to clock errors. Furthermore, δt^{dyn} can be measured from the dt versus t curve, as the point of intersection with the y axis (Fig. 2, bottom right). Both dt/t and δt^{dyn} are independent measurements, and δt^{dyn} can be measured even in the absence of velocity variations dt/t (the dt versus t curve from Fig. 2 is then a horizontal line, but the intersection with the y axis remains δt^{dyn}).

Once the clock difference δt^{dyn} between stations is estimated for all pairs of stations, the clock drift at each station with respect to one master station can be inferred using a least-square inversion similar to what was used for the TSA technique. These estimates of clock errors would be sufficient for correcting the differential travel-time measurements used in earthquake relocation.

An important advantage of the virtual doublet method over TSA is that no assumptions about the NCCF waveform are required. It works if the NCCF is asymmetric or one sided and even when the NCCF has no peak at all (for instance, in the case of very strong scattering), as long as the NCCF is stable over the time of the study. Furthermore, Hadziioannou *et al.* (2009) demonstrated that the cross-correlation function is not required to have converged toward the Green's function for this approach to work, as long as it is stable over the long time scale. Another important strength of the virtual doublet method is the reduced sensitivity to variations in the noise energy distribution that results from removing the direct arrival from the analysis (Brenguier, Campillo, *et al.*, 2008), owing to the smaller sensitivity of scattered waves to the illumination (Gouédard, Roux, *et al.*, 2008).

The virtual doublet method is also more robust against variations in the medium velocity that may occur during the experiment because it looks for stretching in the waveform, which has to be consistent at different times t, whereas the TSA uses only one delay time t, usually corresponding to the most energetic arrival.

The virtual doublet method also has limitations. First, similar to TSA, the resulting clock error estimates are relative to the timing of the reference trace and also to one station of the array considered as the master. Second, absolute errors can be inferred from this technique only if the NCCF is symmetric in time, using the same procedure as for the TSA technique on the reference trace. Third, the accuracy of the clock error measurements is improved compared with TSA by the use of linear regression versus a single measurement, but at the cost of a drop in the resolution in the long time scale (date): because the method is based on the use of late arrivals, it usually requires longer noise records to compute the current day NCCFs. The convergence rate for these late arrivals is indeed smaller than for the direct arrivals, because they correspond to a longer path (Sabra, Gerstoft, *et al.*, 2005; Weaver and Lobkis, 2005).

Application to OBS Data Sets

In this section, we apply the methods described above to two OBS data sets. The differences between these data sets are their duration (20 days against one year) and their nature, the first one being an active experiment (with continuous recordings) and the second being a passive one. We applied TSA to both, but the virtual doublet approach is used only on the long-term deployment. Applying both techniques to this second deployment allows for a side-by-side comparison of their performance.

Data and Preprocessing

The Sismomar Experiment. During the 2005 Sismomar cruise (Singh *et al.*, 2006; Crawford *et al.*, 2010), seismic reflection and refraction data as well as passive seismic measurements were acquired at the Lucky Strike segment of the Mid-Atlantic Ridge to study the role of hydrothermal, tectonic, and magmatic processes in crustal accretion at a slow spreading mid-ocean ridge. A total of 25 OBSs were deployed at 42 sites from the central volcano out to the median valley bounding faults over a period of approximately one month.

In this study, we limit ourselves to the analysis of hydrophone signals from 19 identical instruments. These OBSs operated by the French National Institute of Sciences of the Universe used a Seascan MCXO SISMTB4SC clock and correspond to the L-CHEAPO model developed by the Scripps Institution of Oceanography. The instruments were synchronously deployed in the same locations for a period of ~20 days covering an area of 18×18 km^2 (Fig. 3). The average instrument spacing was 4.5 km, and the instrument depth varied between 1.3 and 2.6 km below sea level. During this part of the experiment, the instruments were sampled at 250 Hz. The drift rate observed after the deployment from GPS synchronization was on the order of ± 0.3 seconds per year.

To prepare the data for the subsequent clock drift analysis, the hydrophone signals were extracted without applying a clock drift correction. This allows for a comparison between the clock drift from GPS measurements at the end of the deployment and the estimated clock drift from TSA. Next, the recordings are downsampled from the original 250 to 10 samples/s. This step saves processing time and ensures a good definition of the low-pass filter. In the subsequent step, the data are filtered in the 2–4 s period band. Although active seismic sources are clearly observable at higher frequencies (Fig. 4), these signals are not visible in the chosen frequency band, and only ambient noise remains in the seismic records. These preprocessed signals are then cross correlated between every available pair of stations in one-day-long records to form the daily NCCFs.

The Gofar Experiment. During the QDG transform fault experiment (Yao *et al.*, 2011; McGuire *et al.*, 2012), 40 seismometers were deployed on the equatorial EPR for a period of one year in 2008 to study the seismicity of oceanic transform faults. The QDG fault system offsets the EPR by 400 km between 3.5° and 5° S. Each fault zone is broken up into multiple secondary active segments, separated by short intratransform spreading centers that range in length from 5 to 16 km (Searle, 1983). The seismometers were a

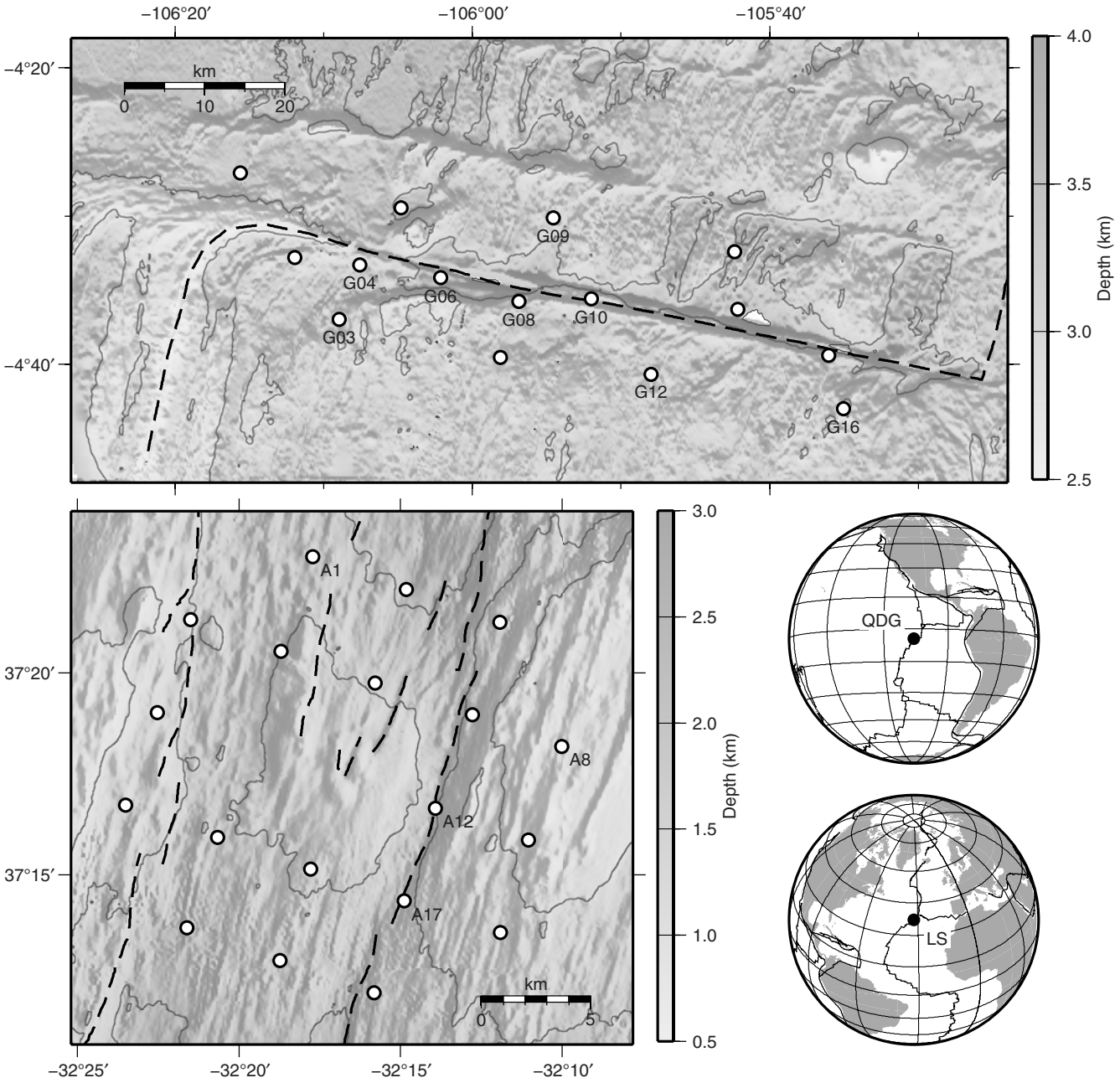

Figure 3. Maps of the Gofar (top, limited to the westernmost segment of the Gofar transform fault) and Sismomar (bottom left) experiments. The circles give the location of the OBS. The dashed lines mark major fault systems of the Lucky Strike segment on the Mid-Atlantic Ridge and the ridge axis and Gofar transform fault in the QDG area. The small globes show the locations of the QDG fault system and the Lucky Strike (LS) segment, with lines marking major plate boundaries (Müller *et al.*, 1997).

mix of broadband Güralp CMG3Ts, Episensor accelerometers, differential pressure gauges, and short-period geophones. The primary goals of the experiment were earthquake source studies, hence the instruments were clustered into several arrays that targeted specific fault segments with typical station spacings of 10–15 km. We will concentrate our analysis on the westernmost segment of the Gofar transform fault (Fig. 3). McGuire *et al.* (2012) performed a large-scale, waveform-based, relocation study of ~25,000 earthquakes on this particular segment in a five-month time period. This was a technically challenging effort due to temporal changes in the medium properties, rotations of the sensors due to strong ground shaking, and clock drifts that exceeded the precision of the waveform derived earthquake differential arrival times (~50 ms). In order to examine the nonlinear clock drift on the Gofar data set in hopes of improving the precision of earthquake locations on this fault, both TSA and the virtual doublet technique were used. The data used for these measurements already have been corrected for a linear clock drift using the GPS measurements.

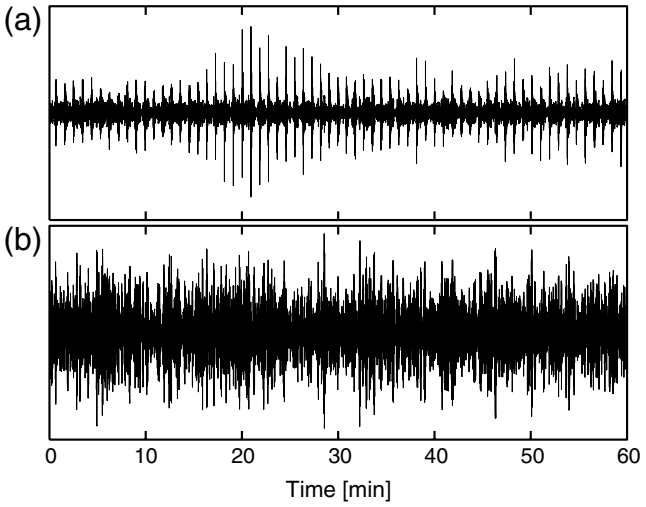

Figure 4. (a) One hour of the original recording at hydrophone A12 from the Sismomar experiment. The signals coming from active shots can be seen as periodic peaks, in which the amplitude depends on the source–receiver distance. (b) The same signal filtered in the 2–4 s period band. The active sources do not produce significant energy in this frequency band.

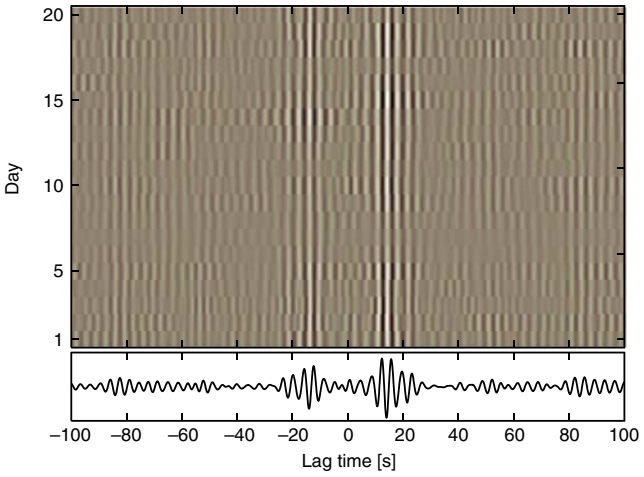

Figure 5. Noise cross-correlation functions for each day at the pair of receivers A1–A17 in the Sismomar experiment in the 2–4 s period band. The bottom trace represents the average over the 20 days of the experiment, which is used as a reference. The color version of this figure is available only in the electronic edition.

Computation of NCCF. Both methods presented in this paper are based on the analysis of NCCFs. We detail here how these are computed. Noise records are first filtered in the selected frequency bands. One-bit normalization (e.g., Larose *et al.*, 2004) is used for the Gofar data set to ensure minimal contamination from earthquake signals, but not for the Sismomar data set because it reduces the convergence rate of the NCCFs and also because the short-duration experiment is easier to check manually for the absence of earthquake signals. NCCFs are computed from one-day-long noise records and normalized by the records' energy (the amplitude of the NCCF is then a correlation coefficient). The daily NCCFs are averaged over one month for the Gofar experiment as the longer interstation distances makes the convergence toward a stable NCCF slower.

Time Symmetry Analysis

We applied TSA to both data sets, but only the application to the Sismomar experiment will be described in detail. Application to the Gofar data set was done using the same processing parameters except for using monthly NCCFs instead of daily ones for Sismomar.

For each pair of receivers, the NCCFs are computed for each day. As shown in Figure 5, they are stable over the course of the experiment and are symmetric in time (at least in phase, if not in amplitude). This is a first indication that the incident energy distribution is reasonably isotropic and that it does not significantly vary over date in the considered frequency band. Fluctuations of arrival times on the positive (dt^+) and negative (dt^-) sides are inferred separately using a reference defined as the stack of the NCCFs over the 20 days of the experiment. Traces are first windowed in time around the amplitude maximum of the reference—separately for positive (s^+) and negative (s^-) times. Shifts in time for each daily NCCF with respect to the reference are measured using a correlation approach, with quadratic interpolation around the maximum to achieve subsample resolution. The symmetry of the variations of dt^+ and dt^- is checked to ensure the lack of illumination-related effects. Time shifts from the positive and negative sides are averaged for each day to give the clock difference with respect to the arbitrary reference for this day, following $\delta t^{\mathrm{dyn}} = (dt^+ - dt^-)/2$. Finally, the absolute clock error δt^{abs} of the reference is determined by comparing the shift between its positive and negative sides as described earlier in the Methods section. These measurements for all pairs are inverted to provide the clock drift for each day and at each station with respect to the master station A8 (Fig. 6). All the instruments were synchronized to GPS time at the time of their deployment, and the clock error should be small at the beginning of the experiment. However, Figure 6 shows large clock errors at the beginning of the experiment. This discrepancy is an indication that the static clock error is not accurately retrieved, due to an insufficient duration of averaging, which results in differences in the waveforms between the positive and negative times in the reference. The cross-correlation method used to assess the static error is very sensitive to these differences, hence the inaccurate retrieval of the absolute clock error.

As mentioned above, performing numerous iterations does not improve the accuracy of the timing error measurements. It can, however, be used to assess the accuracy of the method, because after a large number of iterations the measured error is expected to be zero (we recall that the errors are corrected for after each iteration). Because of measurement noise this is not the case in practice, and the standard deviation of the measured timing error—for one pair of receivers, as a function of the number of iterations—reaches

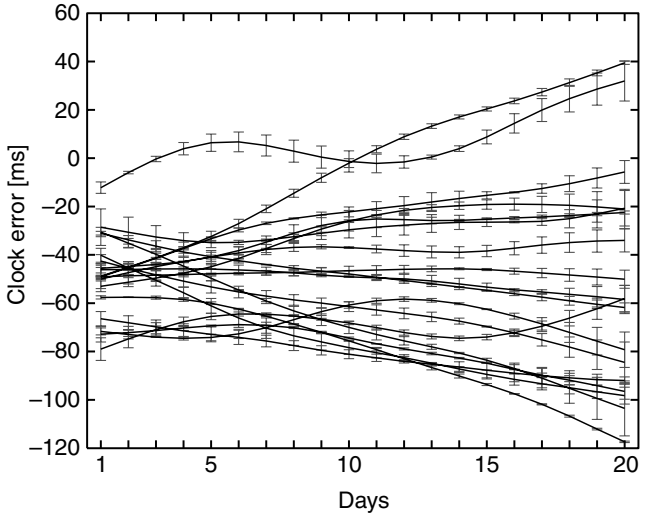

Figure 6. Clock difference for 18 OBSs relative to the nineteenth one (A8) of the Sismomar experiment, as a function of the date. The static shift is not as accurate as the relative one, and the vertical placement of each curve is inaccurate.

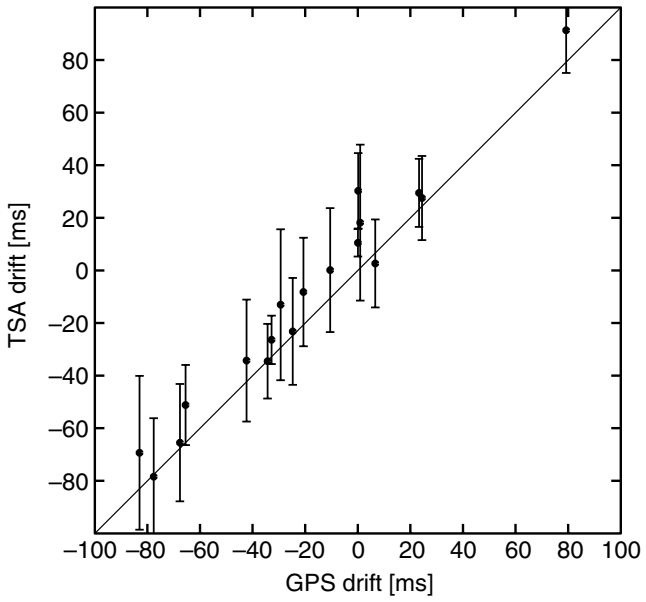

Figure 7. Comparison of accumulated clock drifts from GPS measurements (*x* axis) and from noise-based measurements using TSA (*y* axis) for 18 OBSs with respect to the 19th one (A8). The black line indicates the one-to-one expected ratio.

a plateau. From the value of this plateau the resolution of the method is estimated to be 5 ms, which is small in view of the 10 samples/s sampling rate and the 2–4 s period band. This value is consistent with the error estimates based on the 90% confidence interval as described in the Methods section.

The timing errors presented in Figure 6 can be compared with GPS measurements of clock drift made at the time of each instrument's retrieval. As discussed in the Introduction, the standard procedure to correct for clock drift in OBS studies is to interpolate the drift linearly between the beginning and the end of the experiment. The linear clock drift approximation is acceptable for this short-duration experiment. For comparison with our results, a reference clock error is estimated for each station on the first and the last day of the experiment (which does not exactly coincide with the deployment and retrieval dates) from the GPS measurements. As discussed above, the estimate of the static error is inaccurate, so we compare the GPS measurements of the drift with the estimate of total clock deviation (with respect to one station) accumulated during the 20 days of the experiment (last minus first point of each curve in Fig. 6). Figure 7 shows the agreement between our estimates and the GPS reference is very good, which validates the TSA approach to measure the clock drifts.

This method should work at any frequency (as long as the NCCFs are stable and symmetric), and measurements in different frequency bands can be combined to improve accuracy. This allows the selection of a convenient frequency band, depending on the data set, and in particular one outside of the dominant source spectra in the case of the active survey presented here. We also stress that the achieved resolution of 5 ms is much lower than the period range utilized to make the measurements.

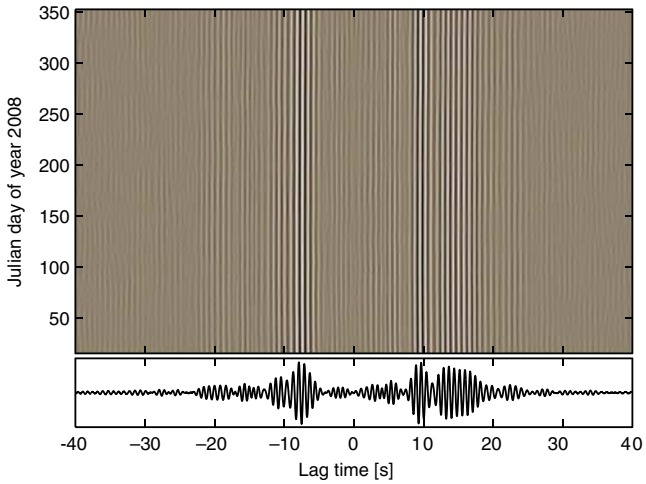

Figure 8. Correlation panel in the 1–2 Hz frequency band for the pair of receivers G04–G06 in the Gofar experiment. Each correlation is averaged over one month centered on the indicated Julian day. The trace at the bottom is the stack over the whole year, which is used as a reference. The color version of this figure is available only in the electronic edition.

Virtual Doublet Analysis

The virtual doublet method is applied to the Gofar experiment in four different frequency bands: 0.5–1 Hz, 1–2 Hz, 2–3 Hz, and 3–4 Hz. Year-long NCCFs functions (stacked against a one-month moving window) obtained in the 1–2 Hz frequency band for OBS pair G04–G06 are presented in Figure 8. Processing parameters, which are

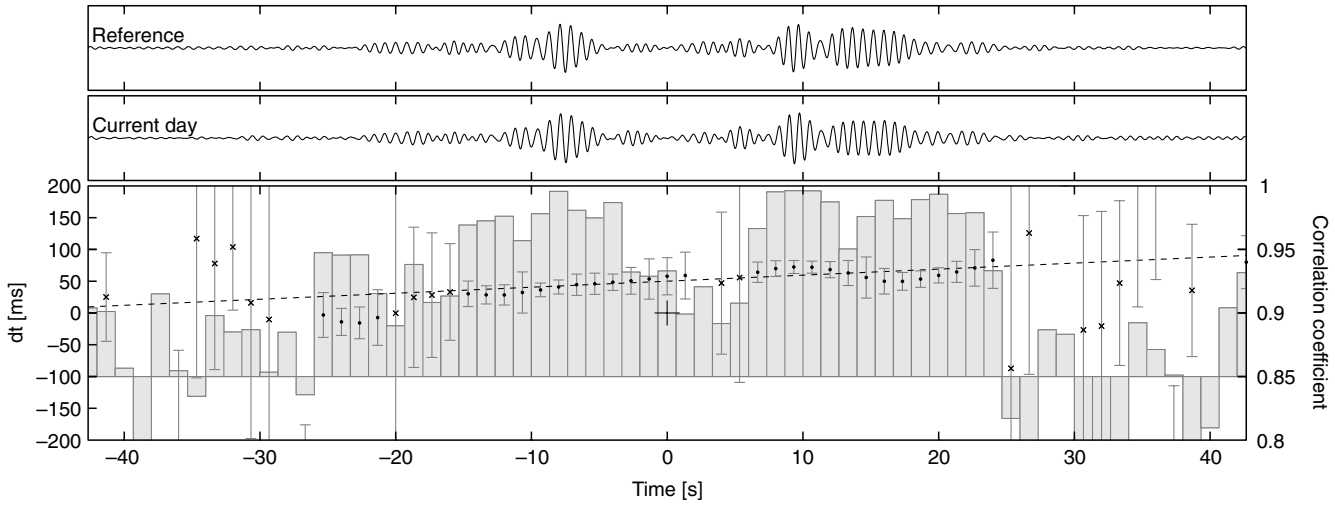

Figure 9. *dt* measurements for day 295 on the G04–G06 OBS pair of the Gofar experiment (real-life equivalent of the left column of Fig. 2). The two top plots show the reference correlation and the NCCF for day 295. The bottom panel shows the *dt*s as a function of correlation lag time *t*, among which some are selected (dots) and some are not (crosses) for the dt/t linear fit (dashed line), based on the correlation coefficient for the two traces in the corresponding window (bar plot, plotted against the 0.85 threshold, *y* scale on the right) and the 90% confidence interval (error bars). The clock difference between the two OBSs for this day is measured as the vertical offset between the dashed line and the (0,0) plot origin (large cross).

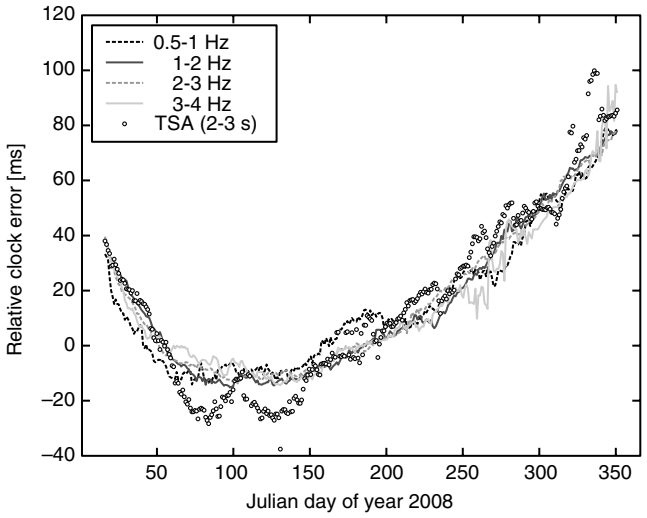

Figure 10. Virtual doublet results for the G04–G06 geophone pair in different frequency bands, along with results from TSA in the 2–3 s period band (shifted vertically to match the average plot).

identical in all frequency bands, are as follows (see also McGuire *et al.*, 2012):

- the reference *r* is defined as a stack of NCCFs from days 1 to 237 (to avoid any possible perturbation from an earthquake that occurred on day 262; McGuire *et al.*, 2012);
- *dt*s are measured in 10-period-long moving Gaussian windows using a cross-correlation approach in the frequency domain;
- *dt*s are used in the linear fit only if the correlation coefficient between the reference and the current NCCF in the corresponding window exceeds 0.85 and if the error on the measurement (width of the 90% confidence interval) is smaller than 100 ms; and
- selected *dt*s are weighted in the linear regression used to infer dt/t according to the squared inverse of their estimated measurement error.

Figure 9 illustrates this process for station pair G04–G06, on a day when there is a velocity difference dv/v between the reference and the NCCF (slope in the *dt* versus *t* plot). Notice that the velocity variation does not affect the clock difference estimate (see Fig. 2).

Measured clock differences at a pair of stations, in the four selected frequency bands, are presented in Figure 10. All measurements agree and could be averaged to improve accuracy. This agreement when using nonoverlapping frequency bands also gives confidence in the accuracy of the measurements. Figure 10 also shows the dynamic clock error for this same data set measured using TSA in the 2–3 s period band (the curve was shifted vertically to align with the virtual doublet measurements, which does not include a static correction). Here again, measurements are in good agreement.

Because the Gofar data set has already been corrected for a linear clock drift using GPS synchronization, the first and last clock offset measurements in Figure 10 should be equal and, ideally, zero. The latter is not verified because only dynamic errors are plotted, and each curve can be shifted vertically by an arbitrary amount corresponding to the static errors. This static error is a constant correction over time corresponding to the absolute timing of the zero of the dynamic time shift (which is relative to an arbitrary date). It includes all drifts that occur before the first measurement point and after the last measurement point of the dynamic shift. However, the ~40 ms difference between the first and the last points is unexpected. A possible explanation for the

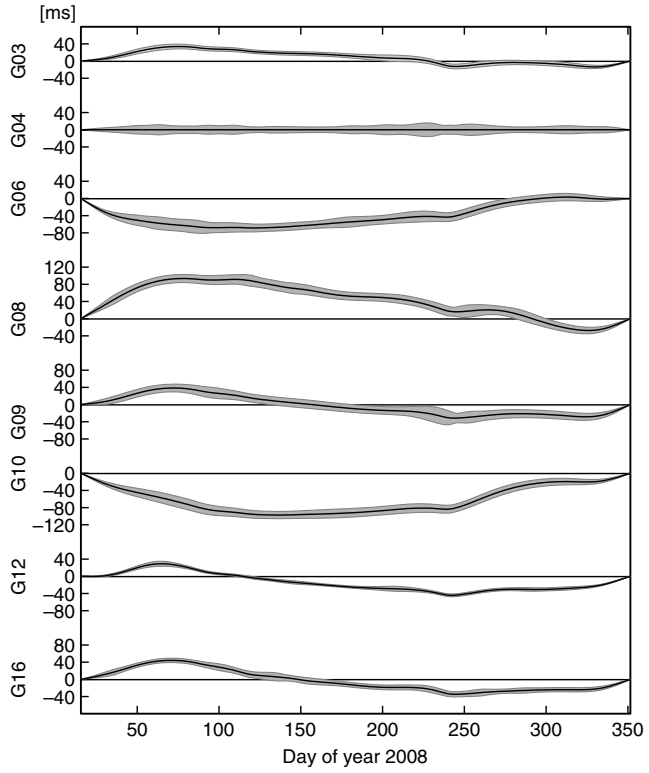

Figure 11. Estimated clock error in ms at each station of the Gofar network, with respect to the arbitrary reference station G04, in the 1–2 Hz frequency band. The gray shaded areas indicate standard deviations from the bootstrapping procedure. Small standard deviation might come from lack of data (due for instance to bad quality NCCFs). OBSs with no data for the main part of the year are removed from the inversion.

deployment process is that after synchronization of their clocks on the ship, the instruments descend ~3 km and undergo a 300-fold increase in pressure and an ~20°C decrease in temperature. Despite the short descent duration (~1 h 15 min at ~40 m/min), the clock response to this brutal environmental change could explain the ~40 ms difference between the first and last points of Figure 10 (Gardner and Collins, 2012; also considering the same change occurs at retrieval).

Asynchronous deployment and retrieval of OBSs could also explain this difference. Deployment of the QDG network took place on 23–26 December 2007 and retrieval on 20–24 January 2009. All clocks are synchronized at deployment time, but by the time the last instrument is put to sea, the clock of the first one has already started to drift (and, again, the same is true about the retrieval process). Furthermore, because the first point of Figure 10 represents the difference in clock between G04 and G06 at a date around 15 January 2008 (first available data point is on 1 January, but the center of the one-month stacking duration is on 15 January), perfect synchronization is not guaranteed any more. The clock drifts obtained from a GPS reference upon retrieval are up to ±2.25 s, which gives maximum linear drift rates of ±2 seconds per year (the mean of the absolute values of drift rates at all OBSs is 0.8 seconds per year). These estimated drift rates, along with deployment and retrieval duration and delay before first measurements, can explain the ~40 ms difference observed in Figure 10.

Once the clock difference is estimated for each pair of stations and each day, the clock at each station can be corrected with respect to one assumed stable, as displayed in Figure 11, in which G04 is used as the master station. In this process, we again applied smoothness regularization, which minimizes the second derivative of the timing error with respect to the date. We also forced the error to be zero at the beginning and the end of the experiment, despite the aforementioned discrepancy.

We used a bootstrapping procedure to estimate the uncertainty on the clock errors. Residuals from a first inversion are randomly permuted and added to the initial *dt* estimates for all pairs to yield a new set of input parameters from which we perform a new inversion. This process is repeated 200 times, thus providing 200 clock error estimates for each station and each day. Final clock errors are then computed as the means of these 200 estimates and the uncertainties as the associated standard deviations. Small standard deviation might result from lack of data to constrain the results, as it is the case for stations G03, G12, and G16 in Figure 11.

Discussion

Both methods presented in this paper allow the postdeployment recovery of the complete (linear and nonlinear) clock drift from NCCFs. Although they both deliver comparable results, each of the methods has strengths and weaknesses, which we will discuss in more detail below.

Accuracy of the Static Clock Shift Estimate

Although the dynamic clock shift is recovered with high precision, the same is not true for the static clock shift. Estimation of the static shift relies on the symmetry of the reference NCCF (usually the stack of all NCCFs over the duration of the experiment), so that timing differences between the positive and negative side can be accurately measured. This symmetry is rarely perfectly achieved due to insufficient averaging and lack of perfectly isotropic illumination.

When considering the virtual doublet approach, the static time shift is furthermore based on a single time difference measurement, whereas dynamic time shifts are estimated using a more robust weighted linear regression.

For these reasons, the static information was not used in this paper, and all clock information is instead relative to the clock of the master station at one arbitrary unknown date (i.e., the definition of zero error). This fully synchronizes the sensors within an array, and is sufficient when using only this array. When using multiple arrays that cannot be synchronized using our approach (e.g., combination with an onshore array), absolute timing is required. Assuming small errors at deployment time and one clock is perfect (e.g.,

the one with the less overall drift as done for Fig. 11) can help overcome the inaccuracy of the static shift estimates.

It is worth mentioning that for methods based on relative arrival times, such as double-difference relocation and double-difference tomography, retrieving the static error is not necessary, and the time series in Figures 6 and 11 can be used directly to correct the differential time measurements for clock errors.

Resolution in the Long Time Scale (Date)

For both methods, the resolution in the long time scale (date) depends on the properties of the noise (such as its azimuthal energy distribution, frequency, and modal content). TSA requires (near) isotropic illumination in order to produce two-sided (and ideally symmetric) NCCFs, whereas the virtual doublet technique can be applied even if the NCCFs do not converge toward the Green's function (Hadziioannou *et al.*, 2009).

When all illumination requirements are fulfilled, TSA has a superior resolution in the long time scale (i.e., shorter noise records are needed) because it only requires the retrieval of a single wave in the NCCF (usually the more energetic direct surface waves), for which convergence is faster than for the later (coda) arrivals (Sabra, Roux, and Kuperman, 2005). The accuracy of the measurements is, however, more sensitive to any variation in the illumination.

Accuracy in the Short Time Scale (Timing Errors)

Accuracy in the short time scale depends on the specific waveforms used for tracking misalignments dt in the NCCFs, and in particular their frequency content. Using longer periods might affect the resolution in dt because of inaccuracy in the definition of the maximum in the correlation-based measurement of the time shift. However, because the relevant information for both methods is dt/t, how the accuracy on the dynamic error depends on the signal frequency is not straightforward (and even more so for the virtual doublet approach). Stehly *et al.* (2007) reported a resolution on dynamic time shifts of less than 1% of the wave period using a method close to the TSA approach presented in this paper. The virtual doublet technique has a better resolution on the value of the clock error (short time scale) because it uses a linear regression to infer dt/t rather than a single time difference estimate. This is illustrated by Figure 10, in which the TSA measurements fluctuate more than the virtual doublet measurements.

In practice, combined with the long-time-scale resolution, this means that for the Gofar experiment switching from a 30-day NCCF to a 5-day NCCF (i.e., asking for a higher long-time-scale resolution) would be possible using the TSA approach, as this would be enough to reconstruct the direct surface waves. This would, however, not be possible with virtual doublets because the later arrivals (coda waves) would not have sufficient signal-to-noise ratio and, hence, the dts would not be measurable on a wide-enough range of ts to perform a meaningful linear regression. The measurement error using TSA would nevertheless be large (i.e., poor short-time-scale accuracy). By increasing the duration of the noise records used in the NCCF computation, this measurement error decreases. The virtual doublet measurements would also become possible and would provide measurements with better short-time-scale accuracy.

Validation of Time-Shift Measurements

Estimates of the overall linear clock drift made with the TSA method are consistent with those inferred from GPS synchronization (Fig. 7). The nonlinear clock error estimates are, however, more difficult to validate because there is no easy reference for comparison. To do so, we compared the five independent measurements in Figure 10 (TSA and the virtual doublet technique in four nonoverlapping frequency bands). The good agreement between all the measurements increases our confidence in the clock differences and the nonlinear clock drift presented in Figure 11.

Implications for OBS Deployments

We found the typical magnitude for the nonlinear drift (∼100 ms/yr peak to peak from Fig. 7) to be about 10 percent of the average linear drift (∼1 s/yr). We conclude that the nonlinear component of the clock drift can be neglected for short time deployments (how short will depend on the timing accuracy required for the processing, but a one-month duration is a good mark given observed drift rates) in which the usual correction for a linear drift performs well. This neglects the duration-independent (at deployment and retrieval) response of the clock to environmental changes, which might differ from one instrument to another, and cannot be evaluated without an absolute time reference while the instruments are at sea (and not usually available).

We emphasize the variety in frequency bands utilized in this paper. In practice, any frequency band in which the waveform has suitable properties would work, giving flexibility for the application of these methods. This variety of frequency bands allows an equal variety of interstation spacings, as the convergence rate of the NCCF is linked to the wavelength/offset ratio (Sabra, Roux, and Kuperman, 2005), and noise correlation approaches have been applied successfully to a wide range of scales (e.g., Stehly *et al.*, 2007; Gouédard, Stehly, *et al.*, 2008; Hadziioannou *et al.*, 2009; Yao *et al.*, 2011). We also note that both methods could be used on all the nine components of the correlation tensor (for three component raw records) and could also use accelerometers or hydrophones when available as was the case for the Sismomar experiment. Combining different components and frequency bands would further increase the accuracy of the method.

Conclusions

We demonstrated that both the linear and nonlinear drifts of instrumental OBS clocks can be measured postdeployment from the analysis of NCCFs. The estimated magnitude of the nonlinear component of the timing errors are one order of magnitude smaller than the linear component, but they are higher or comparable to the residuals from modern earthquake relocation studies. Hence, the ability to estimate and remove these errors will be the key for maximizing the scientific utility of OBS data sets. The wide range of allowed acquisition and processing parameters (frequency band, network aperture, typical interstation offsets) makes the analysis of NCCFs a versatile tool for the validation and quality control of continuous recordings. The methods presented in this paper can improve resolution in a wide range of passive seafloor seismic experiments. The proposed virtual doublet analysis relaxes assumptions about the recorded wavefield compared with the TSA method, but this comes at the cost of lower resolution of clock errors with respect to the long time scale (date). The ∼1 month resolution is, however, acceptable with respect to the characteristic drift rates of instrumental clocks.

Data and Resources

The Quebrada–Discovery–Gofar transform experiment, of which the Gofar data set is part, has been carried out by the Woods Hole Oceanographic Institution, and data are publicly available from the Incorporated Research Institution for Seismology (IRIS) Data Management Center at www.iris.edu. More information about ocean-bottom seismometer (OBS) experiments are available at the National Science Foundation's Ocean-Bottom Seismometer Instrument Pool website (http://www.obsip.org). The Sismomar experiment has been carried out by the Institut de Physique du Globe de Paris, using OBSs from the Institut National des Sciences de l'Univers instrument pool. Figure 3 was made using the Generic Mapping Tool (www.soest.hawaii.edu/gmt; Wessel and Smith, 1998). All URLs mentioned in this paper were last accessed June 2013.

Acknowledgments

We thank Amber Stangroom, a Massachusetts Institute of Technology (MIT) undergraduate, for her help initiating this work. P. G. was supported by a Shell Research grant during his stay at MIT. He thanks his new employer, Magnitude LLC, for letting him take the required time to finish this work. We would like to thank all participants of the Sismomar cruise, as well as crew and captain of the French research vessel N/O L'Atalante. Many of the Woods Hole Oceanographic Institution instruments for the Gofar experiment were constructed with funding from the W. M. Keck Foundation. Finally, we thank the Associate Editor and two anonymous reviewers for their helpful suggestions.

References

Brenguier, F., M. Campillo, C. Hadziioannou, N. M. Shapiro, R. M. Nadeau, and E. Larose (2008). Postseismic relaxation along the San Andreas fault at Parkfield from continuous seismological observations, *Science* **321,** no. 5895, 1478–1481.

Brenguier, F., N. M. Shapiro, M. Campillo, Z. Ferrazzini, Z. Duputel, O. Coutant, and A. Nercessian (2008). Towards forecasting volcanic eruptions using seismic noise, *Nature Geosci.* **1,** no. 1, 126–130.

Campillo, M. (2006). Phase and correlation in 'random' seismic fields and the reconstruction of the Green function, *Pure Appl. Geophys.* **163,** nos. 2/3, 475–502.

Campillo, M., and A. Paul (2003). Long-range correlations in the diffuse seismic coda, *Science* **299,** 547–549.

Clarke, D., L. Zaccarelli, N. M. Shapiro, and F. Brenguier (2011). Assessment of resolution and accuracy of the moving window cross spectral technique for monitoring crustal temporal variations using ambient seismic noise, *Geophys. J. Int.* **186,** no. 2, 867–882.

Constable, S. C., R. L. Parker, and C. G. Constable (1987). Occam's inversion: A practical algorithm for generating smooth models from electromagnetic data, *Geophysics* **52,** no. 3, 289–300.

Crawford, W. C., S. C. Singh, T. Seher, V. Combier, D. Düsünür, and M. Cannat (2010). Crustal structure, magma chamber, and faulting beneath the Lucky Strike hydrothermal vent field, in *Diversity of Hydrothermal Systems on Slow Spreading Ocean Ridges*, P. Rona, C. Devey, J. Dyment, and B. Murton (Editors), Geophysical Monograph Series, Vol. 188, American Geophysical Union, 113–132.

deMartin, B. J., R. A. Sohn, J. P. Canales, and S. E. Humphris (2007). Kinematics and geometry of active detachment faulting beneath the Trans-Atlantic Geotraverse (TAG) hydrothermal field on the Mid-Atlantic Ridge, *Geology* **35,** no. 8, 711–714.

Düsünür, D., J. Escartín, V. Combier, T. Seher, W. Crawford, M. Cannat, S. C. Singh, L. M. Matias, and J. M. Miranda (2009). Seismological constraints on the thermal structure along the Lucky Strike segment (Mid-Atlantic Ridge) and interaction of tectonic and magmatic processes around the magma chamber, *Marine Geophys. Res.* **30,** no. 2, 105–120.

Froment, B., M. Campillo, P. Roux, P. Gouédard, A. Verdel, and R. L. Weaver (2010). Estimation of the effect of non-isotropically distributed energy on the apparent arrival time in correlations, *Geophysics* **75,** no. 5, SA85–SA93.

Gardner, A. T., and J. A. Collins (2012). Advancements in high-performance timing for long term underwater experiments: A comparison of chip scale atomic clocks to traditional microprocessor-compensated crystal oscillators, in *Oceans, 2012*, 1–8, doi: 10.1109/OCEANS.2012.6404847.

Gouédard, P., P. Roux, M. Campillo, and A. Verdel (2008). Convergence of the two-point correlation function toward the Green's function in the context of a seismic prospecting data set, *Geophysics* **73,** no. 6, V47–V53.

Gouédard, P., L. Stehly, F. Brenguier, M. Campillo, Y. Colin de Verdière, E. Larose, L. Margerin, P. Roux, F. J. Sánchez-Sesma, N. M. Shapiro, and R. L. Weaver (2008). Cross-correlation of random fields: Mathematical approach and applications, *Geophys. Prospect.* **56,** no. 3, 375–393.

Hadziioannou, C., E. Larose, O. Coutant, P. Roux, and M. Campillo (2009). Stability of monitoring weak changes in multiply scattering media with ambient noise correlation: Laboratory experiments, *J. Acoust. Soc. Am.* **125,** no. 6, 3688–3695.

Larose, E., J. de Rosny, L. Margerin, D. Anache, P. Gouédard, M. Campillo, and B. A. van Tiggelen (2006). Observation of multiple scattering of kHz vibrations in a concrete structure and application to monitoring weak changes, *Phys. Rev. E* **73,** no. 1, 016609.

Larose, E., L. Margerin, B. A. van Tiggelen, and M. Campillo (2004). Weak localization of seismic waves, *Phys. Rev. Lett.* **93,** no. 4, 048501.

Lin, G., P. M. Shearer, and E. Hauksson (2008). A search for temporal variations in station terms in southern California from 1984 to 2002, *Bull. Seismol. Soc. Am.* **98,** no. 5, 2118–2132.

McGuire, J. J., J. A. Collins, P. Gouédard, E. Roland, D. Lizarralde, M. S. Boettcher, M. D. Behn, and R. D. van der Hilst (2012). Variations in earthquake rupture properties along the Gofar transform fault, East Pacific Rise, *Nature Geosci.* **5,** 336–341.

Müller, R. D., W. R. Roest, J.-Y. Royer, L. M. Gahagan, and J. G. Sclater (1997). Digital isochrons of the world's ocean floor, *J. Geophys. Res.* **102,** no. B2, 3211–3214.

Poupinet, G., W. L. Ellsworth, and J. Fréchet (1984). Monitoring velocity variations in the crust using earthquake doublets: An application to the Calaveras fault, California, *J. Geophys. Res.* **89,** no. B7, 5719–5731.

Poupinet, G., J.-L. Got, and F. Brenguier (2008). Monitoring temporal variations of physical properties in the crust by cross-correlating the waveforms of seismic doublets, in *Advances in Geophysics*, Vol. 50, Elsevier, 373–399, doi: 10.1016/S0065-2687(08)00014-9.

Rubin, A. (2002). Using repeating earthquakes to correct high-precision earthquake catalogs for time-dependent station delays, *Bull. Seismol. Soc. Am.* **92,** no. 5, 1647–1659.

Rubin, A., and D. Gillard (2000). Aftershock asymmetry/rupture directivity among central San Andreas fault microearthquakes, *J. Geophys. Res.* **105,** no. B8, 19,095–19,109.

Rubin, A., D. Gillard, and J. Got (1999). Streaks of microearthquakes along creeping faults, *Nature* **400,** no. 6745, 635–641.

Sabra, K. G., P. Gerstoft, P. Roux, W. A. Kuperman, and M. C. Fehler (2005). Surface wave tomography from microseisms in southern California, *Geophys. Res. Lett.* **32,** L14311, doi: 10.1029/2005GL023155.

Sabra, K. G., P. Roux, and W. A. Kuperman (2005). Emergence rate of the time-domain Green's function from the ambient noise cross-correlation, *J. Acoust. Soc. Am.* **118,** no. 6, 3524–3531.

Sánchez-Sesma, F. J., and M. Campillo (2006). Retrieval of the Green's function from cross correlation: The canonical elastic problem, *Bull. Seismol. Soc. Am.* **96,** no. 3, 1182–1191.

Sánchez-Sesma, F. J., J. A. Pérez-Ruiz, M. Campillo, and F. Luzón (2006). Elastodynamic 2-D Green function retrieval from cross-correlation: Canonical inclusion problem, *Geophys. Res. Lett.* **33,** L13305, doi: 10.1029/2006GL026454.

Schaff, D., G. Bokelmann, G. Beroza, F. Waldhauser, and W. Ellsworth (2002). High-resolution image of Calaveras fault seismicity, *J. Geophys. Res.* **107,** no. B9, 2186.

Schaff, D. P., G. H. R. Bokelmann, W. L. Ellsworth, E. Zanzerkia, F. Waldhauser, and G. C. Beroza (2004). Optimizing correlation techniques for improved earthquake location, *Bull. Seismol. Soc. Am.* **94,** no. 2, 705–721.

Searle, R. C. (1983). Multiple, closely spaced transform faults in fast-slipping fracture-zones, *Geology* **11,** no. 10, 607–610.

Sens-Schönfelder, C. (2008). Synchronizing seismic networks with ambient noise, *Geophys. J. Int.* **174,** no. 3, 966–970.

Sens-Schönfelder, C., and U. Wegler (2006). Passive image interferometry and seasonal variations of seismic velocities at Merapi volcano, Indonesia, *Geophys. Res. Lett.* **33,** no. 21, L21302, doi: 10.1029/2006GL027797.

Shapiro, N. M., and M. Campillo (2004). Emergence of broadband Rayleigh waves from correlations of the ambient seismic noise, *Geophys. Res. Lett.* **31,** L07614, doi: 10.1029/2004GL019491.

Singh, S. C., W. C. Crawford, H. Carton, T. Seher, V. Combier, M. Cannat, J. P. Canales, D. Düsünür, J. Escartín, and J. M. Miranda (2006). Discovery of a magma chamber and faults beneath a Mid-Atlantic Ridge hydrothermal field, *Nature* **442,** no. 7106, 1029–1032.

Stehly, L., M. Campillo, and N. M. Shapiro (2007). Travel time measurements from noise correlation: Stability and detection of instrumental time-shifts, *Geophys. J. Int.* **171,** no. 1, 223–230.

Stroup, D. F., M. Tolstoy, T. J. Crone, A. Malinverno, D. R. Bohnenstiehl, and F. Waldhauser (2009). Systematic along-axis tidal triggering of microearthquakes observed at 9° 0′ N East Pacific Rise, *Geophys. Res. Lett.* **36,** L18302, doi: 10.1029/2009GL039493.

Tarantola, A. (2005). *Inverse Problem Theory and Methods for Model Parameter Estimation*. Society for Industrial and Applied Mathematics, Philadelphia, Pennsylvania.

Tolstoy, M., F. Waldhauser, D. R. Bohnenstiehl, R. T. Weekly, and W. Y. Kim (2008). Seismic identification of along-axis hydrothermal flow on the East Pacific Rise, *Nature* **451,** no. 7175, 181–184.

Tsai, V. C. (2009). On establishing the accuracy of noise tomography travel-time measurements in a realistic medium, *Geophys. J. Int.* **178,** no. 3, 1555–1564.

Wapenaar, K. (2004). Retrieving the elastodynamic Green's function of an arbitrary inhomogeneous medium by cross-correlation, *Phys. Rev. Lett.* **93,** no. 25, 254301.

Weaver, R. L. (2005). Information from seismic noise, *Science* **307,** no. 5715, 1568–1569.

Weaver, R. L., and O. I. Lobkis (2001). Ultrasonics without a source: Thermal fluctuation correlations at MHz frequencies, *Phys. Rev. Lett.* **87,** no. 13, 134301.

Weaver, R. L., and O. I. Lobkis (2005). Fluctuations in diffuse field-field correlations and the emergence of the Green's function in open systems, *J. Acoust. Soc. Am.* **117,** no. 6, 3432–3439.

Weaver, R., B. Froment, and M. Campillo (2009). On the correlation of non-isotropically distributed ballistic scalar diffuse waves, *J. Acoust. Soc. Am.* **126,** no. 4, Part 1, 1817–1826.

Wegler, U., and C. Sens-Schönfelder (2007). Fault zone monitoring with passive image interferometry, *Geophys. J. Int.* **168,** no. 3, 1029–1033.

Wessel, P., and W. H. F. Smith (1998). New, improved version of Generic Mapping Tools released, *Eos Trans. AGU* **79,** 579–579.

Yao, H., and R. D. van der Hilst (2009). Analysis of ambient noise energy distribution and phase velocity bias in ambient noise tomography, with application to SE Tibet, *Geophys. J. Int.* **179,** no. 2, 1113–1132.

Yao, H., X. Campman, M. V. de Hoop, and R. D. van der Hilst (2009). Estimation of surface wave Green's functions from correlation of direct waves, coda waves, and ambient noise in SE Tibet, *Phys. Earth Planet. In.* **177,** nos. 1/2, 1–11.

Yao, H., P. Gouédard, J. A. Collins, J. J. McGuire, and R. D. van der Hilst (2011). Structure of young East Pacific Rise lithosphere from ambient noise correlation analysis of fundamental- and higher-mode Scholte–Rayleigh waves, *Comptes Rendus Geosci.* **343,** nos. 8/9, 571–583.

Massachusetts Institute of Technology
Department of Earth, Atmospheric and Planetary Sciences
77 Massachusetts Avenue
Cambridge, Massachusetts 02139
pierre.gouedard@magnitude-geo.com
(P.G., T.S., R.D.v.)

Woods Hole Oceanographic Institution
266 Woods Hole Road
Woods Hole, Massachusetts 02543
(J.J.M., J.A.C.)

Manuscript received 18 June 2013;
Published Online 15 April 2014